Available online at www.sciencedirect.com
ScienceDirect
Trans. Nonferrous Met. Soc. China 33(2023) 2588−2598
Transactions of Nonferrous Metals Society of China
www.tnmsc.cn

Local microstructure and strengthening mechanisms of double-sided friction stir welded Al−Mg−Mn−Er alloy joint

Hai-bin LIU, Teng-da WANG, Guo-yuan LIU, Shu-feng XIE,
Shao-qi CHU, Bin XIE, Sheng-li YANG, Peng-yun WANG

Luoyang Ship Material Research Institute, Luoyang 471023, China

Received 21 March 2022; accepted 1 June 2022

Abstract: Local microstructure and strengthening mechanisms of double-sided friction stir welded Al−Mg−Mn−Er alloy joint were investigated to reveal its softening mechanism. The results showed that a fine equiaxed grain structure (5.61 μm) was formed in the nugget zone (NZ), while the thermo-mechanically affected zone (TMAZ, 45.32 μm) and heat-affected zone (HAZ, 100.73 μm) maintained a fibrous grain structure. The fraction of low angle grain boundaries decreased from 75.6% of the base metal (BM) to 15.6% of the NZ. The annealing effect resulted in obvious reduction in dislocation density from $1.8\times10^{14}\ m^{-2}$ of the BM to $4.5\times10^{12}\ m^{-2}$ of the NZ. The average diameter size and volume fraction of $Al_3(Er,Zr)$ precipitates of the NZ, TMAZ and HAZ were close to those of the BM (13.7 nm and 0.13%). The NZ and TMAZ exhibited the lowest yield strength of about 201 MPa while the BM had the highest yield strength of about 295 MPa. The loss of the dislocation strengthening and substructure strengthening was the main reason for the decrease of yield strength from the BM to the NZ.
Key words: Al−Mg−Mn−Er alloy; double-sided friction stir welding; microstructure; strengthening mechanisms

1 Introduction

Al−Mg−Mn−Er alloy has been widely used in the construction of ocean ships due to its medium high strength, good deformability and excellent corrosion resistance. To avoid the solidification defects resulted from fusion welding method [1,2], friction stir welding (FSW) has been used to join Al−Mg−Mn−Er alloy plates. Due to the solid-state joining mechanism and the occurrence of dynamic recrystallization [3,4], both the microstructure and mechanical properties of FSW joints are improved.

Compared to single-sided friction stir welding (SSFSW), double-sided friction stir welding (DSFSW) could effectively eliminate the root defects. CABIBBO et al [5] found that the DSFSWed joints of 6082 aluminum alloy exhibited better formability than the SSFSWed joints. XU and LIU [6] showed that DSFSW caused substantial grain refinement in the weld of DSFSWed 7085 aluminum alloy joints. YANG et al [7] proved that the joint coefficient (the ratio of the fracture strength of the joint to that of the base material) of DSFSWed 6082 aluminum alloy ultra-thick plate joints could reach the same level as the SSFSW joints. Based on above studies, it is confirmed that the DSFSWed joints could simultaneously obtain desirable formability and strength properties.

As for work-hardened Al−Mg series alloys, the softening of FSW joints is inevitable and undesirable. Many researchers have analyzed the mechanism of strength loss in the nugget zone (NZ). PENG et al [8] found that the FSWed joints of

Corresponding author: Hai-bin LIU, Tel: +86-15978683591, E-mail: lhb725210@163.com;
Peng-yun WANG, Tel: +86-15194576515, E-mail: wpy_725@126.com
DOI: 10.1016/S1003-6326(23)66283-1

rolled Al−Mg−Sc alloy plates occupied the lowest hardness in the nugget zone (NZ) owing to partial recrystallization and dissolve of a small amount of $Al_3(Sc,Zr)$ particles. HAO et al [9] revealed that the NZ of FSWed Al−Mg−Er alloy sheet joints had the lowest hardness because of the annealing softening caused by welding thermal cycle. MALOPHEYEV et al [10] showed that the loss of dislocation strengthening and substructure strengthening resulted in relatively low strength in the NZ of FSWed joints of work-hardened Al−Mg−Sc−Zr alloys.

However, studying the softening mechanism of the NZ alone is not enough to propose the strengthening measures for FSW joints. As known, the FSW joints show an inhomogeneous microstructure and the mechanism of yield strength loss may change with the distance from the center line of the weld. The video extensometer is an advanced optical device to detect the surface strains of a tensile sample by processing the video/images recorded during loading [11,12]. Theoretically speaking, the engineering stress−engineering strain curves between any two points could be output. Thus, the yield strength loss of different zones could be obtained. Combined with the theoretically calculated yield strength, the softening mechanism from the NZ to the BM (base metal) rather than only the NZ could be revealed.

In the present study, the DSFSW method was used to join Al−Mg−Mn−Er alloy plates. The evolution of contributions of different strengthening mechanisms from the NZ to the BM were quantitatively analyzed. Further, the softening mechanism of different zones of DSFSWed Al−Mg−Mn−Er alloy joint was revealed.

2 Experimental

The H321 state Al−Mg−Mn−Er alloy plates were used in the present study. The chemical composition and mechanical properties are listed in Tables 1 and 2, respectively. The plates were cut into dimensions of 500 mm × 150 mm × 10 mm for welding. The DSFSW process was completed using a HT-JM40×250/1 FSW machine. The tilt angle was 2.5°. To avoid the root defects, the DSFSW was conducted two welding passes, one pass on the top surface and the other on the bottom surface. The welding direction of the two passes was the same. A steel tool with a shoulder of 24 mm in diameter was used. To strengthen the softening effect and reveal the softening mechanism, a conical threaded pin of 9.8 mm in length instead of half of the thickness was used to increase the heat input. Based on preliminary experimental results, the rotation rate and the welding speed were set as 250 r/min and 100 mm/min, respectively. The welding direction was parallel to the rolling direction.

Table 1 Chemical composition of Al−Mg−Mn−Er alloy (wt.%)

Fe	Mg	Mn	Zr	Si	Er	Al
0.122	6.04	0.946	0.100	0.015	0.193	Bal.

Table 2 Mechanical properties of Al−Mg−Mn−Er alloy

Yield strength/MPa	Tensile strength/ MPa	Elongation/ %
297	416	19.5
294	412	16.5

Microstructures of different zones were observed on the transverse cross-section of DSFSWed joint by optical microscopy (OM, ZEISS Observer Z1.m), scanning electron microscopy (SEM, Scios 2) equipped with an electron backscattered diffraction detector (EBSD, Aemtek Materials Analysis Division) and transmission electron microscopy (TEM, JEM−2100, 200 kV). The OM sample was mechanically polished and then etched using 40 vol.% phosphate aqueous solution before observation. The EBSD samples were prepared in a 10 vol.% perchloric acid alcohol solution at 25 V. The TEM samples were prepared by double jet ion thinning in a 30 vol.% nitric acid methanol solution at 25 V.

The OIM software was used to analyze the original EBSD data. The data were obtained using a step size of 0.3−1 μm depending on the grain size. The 15° was used as a critical value to differentiate low-angle grain boundaries (LAGBs) and high-angle grain boundaries (HAGBs). Only grain boundaries with misorientation angles between 2° and 15° was defined as LAGBs to eliminate boundaries caused by orientation noise [6,10]. The grain orientation spread (GOS) not higher than 2° was used to distinguish recrystallization grains and quantify the recrystallization fraction [13−17]. The

Kernel Average Misorientation (KAM) approach was used to estimate the density of geometrically necessary dislocations (GNDs), and the KAM values larger than 2° were excluded to avoid the effect of adjacent grains and subgrains [18−22]. The Image Pro Plus (IPP) software was used to quantify the average diameter size and the volume fraction of $Al_3(Er,Zr)$ precipitates. The statistical number was not less than 100.

The Instron 5985 electron universal testing machine and AVE2-2663-901 video extensometer were used to conduct the tensile tests. According to GB/T 228.1, two tensile samples were tested at room temperature with an initial strain rate of $0.25\times10^{-3}\ s^{-1}$. No more tensile samples were tested due to the similar results. The surfaces of each tensile sample were polished to a roughness of 0.6 μm (R_a) and the thickness was reduced from 10 to 8 mm. The schematic drawing of tensile samples is shown in Fig. 1. The method for generating the yield strength profile is described as follows. From the center of the weld to both sides, different engineering stress−engineering strain curves were output per 1 mm. Each engineering stress−engineering strain curve generated a yield strength which was defined as the average yield strength for the range of 1 mm. Therefore, the yield strength at X point reflected the average yield strength from X-1 point to X point. It is worth noting that the range of 1 mm contains a limited number of grains and the engineering stress−engineering strain curves are distorted to some extent. Although it does not affect the trend, the error of yield strength value is inevitable. More experimental data are required to evaluate the degree of the error.

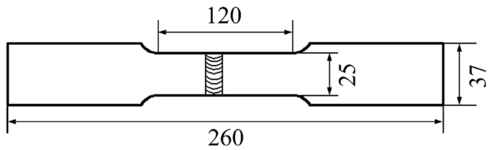

Fig. 1 Schematic drawing of tensile samples (Unit: mm)

3 Results

3.1 Microstructures of different zones

Figure 2 shows the macrostructure of DSFSWed joint of Al−Mg−Mn−Er alloy. The NZ and the TMAZ are distinguished by brighter contrast and plastic flow patterns, respectively. The range of the HAZ is determined by the yield strength profile, as shown in Fig. 7. Due to the double-sided friction stir welding, the swirl zone (SWZ) observed in the SSFSW joints disappears. While the shoulder-driven zone (SDZ) and the pin-driven zone (PDZ) could still be marked due to the roles of the shoulder and pin [9]. Asymmetric morphology is observed in both SDZs. According to the research of BIROL and KASMAN [23], the reason for forming an asymmetrical NZ was that a much lower deformation rate on the RS. The "S" lines are seen in both SDZs, as marked by the red arrows. A similar phenomenon was observed by HAO et al [9] and STATO et al [24]. According to literature [9,24], the "S" lines formed because the oxide film on the butt faces was broken up and arranged during the FSW process as a result of insufficient heat input. Considering a lower heat input in the present work (250 r/min and 100 mm/min vs 400 r/min and 100 mm/min [9]), the formation of "S" lines in both SDZs could be attributed to the same reason.

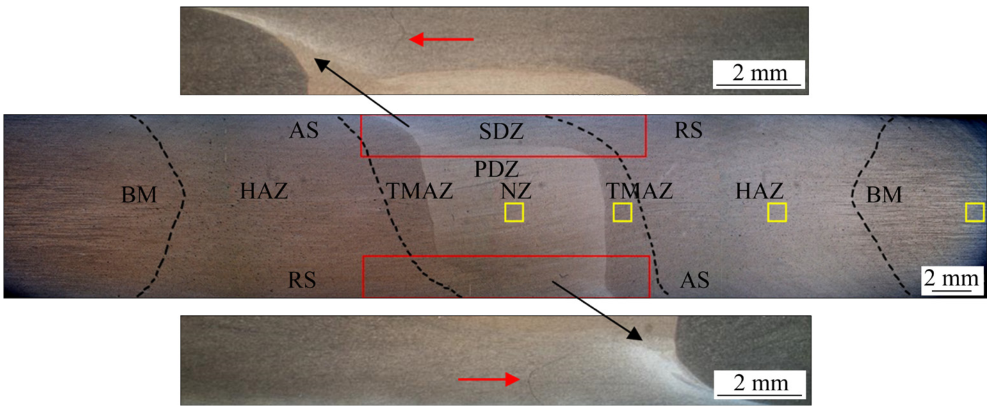

Fig. 2 Macrostructure of DSFSWed joint of Al−Mg−Mn−Er alloy (HAZ−Heat-affected zone; TMAZ−Thermo-mechanically affected zone; AS−Advanced side; RS−Retreated side)

The inverse pole figure (IPF) maps of DSFSWed joint of Al−Mg−Mn−Er alloy are shown in Fig. 3. A fine equiaxed grain structure forms in the NZ, as shown in Fig. 3(a). The average grain size (AGS) of the NZ is 5.61 μm. A mixed structure consisting of coarse fibrous grains and fine equiaxed grains is observed in the TMAZ and HAZ, as shown in Figs. 3(b) and (c). The average grain sizes of the TMAZ and HAZ are 45.32 and 100.73 μm, respectively. The BM has hot-rolled structure and is mainly composed of coarse fibrous and ultrafine grains, and its average grain size is 73.01 μm, as shown in Fig. 3(d).

Figure 4 shows GOS maps of different zones of the DSFSWed joint of Al−Mg−Mn−Er alloy. The quantified recrystallization fractions of the NZ, TMAZ, HAZ and BM are 93.6%, 42.7%, 36.6% and 10.6%, respectively, as marked by orange color in Figs. 4(a−d). In the BM, the recrystallized grains are mainly ultrafine grains formed due to dynamic recrystallization during the hot rolling process. From the BM to the NZ, the recrystallization fraction shows an obvious increasing trend. The HAZ has experienced a temperature rise effect, the growth of ultrafine grains increased the recrystallization fraction. The TMAZ has experienced a stronger temperature rise effect and exhibited a higher recrystallization fraction than the HAZ. The sufficient recrystallization resulted from severe plastic strain occurred in the NZ, which brought about a fine equiaxed grain structure.

In the NZ, the quantified number fraction of LAGBs is obviously lower than that of HAGBs due to sufficient recrystallization in the NZ. In contrast, the quantified number fraction of LAGBs is higher than that of HAGBs in the TMAZ, HAZ and BM. It means that the subgrain boundary strengthening mechanism played an important role in the TMAZ, HAZ and BM.

The low magnification TEM microstructure of the DSFSWed joint of Al−Mg−Mn−Er alloy is shown in Fig. 5. In the NZ (Fig. 5(a)), the Al_6Mn particles are randomly distributed and several fine equiaxed grains are formed due to severe plastic strain. Due to the annealing effect caused by welding thermal cycle, only a few dislocations are observed in the NZ. The TMAZ experienced shearing deformation, so the Al_6Mn particles are

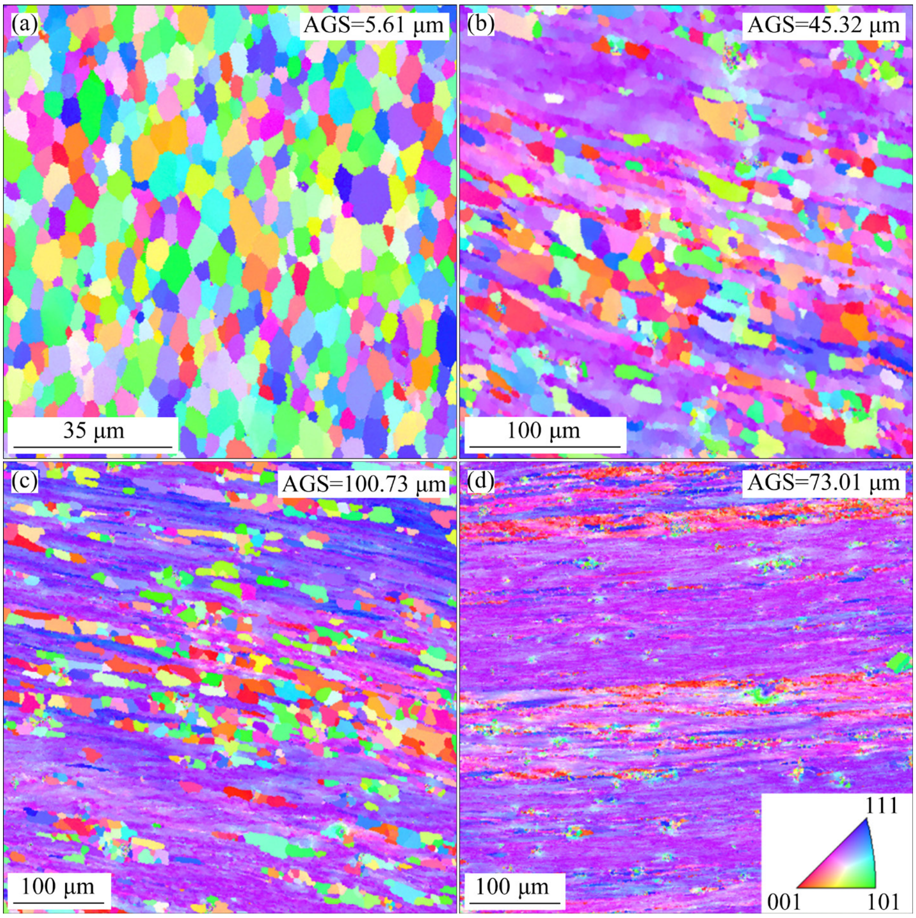

Fig. 3 IPF maps of different zones of DSFSWed joint of Al−Mg−Mn−Er alloy: (a) NZ; (b) TMAZ; (c) HAZ; (d) BM

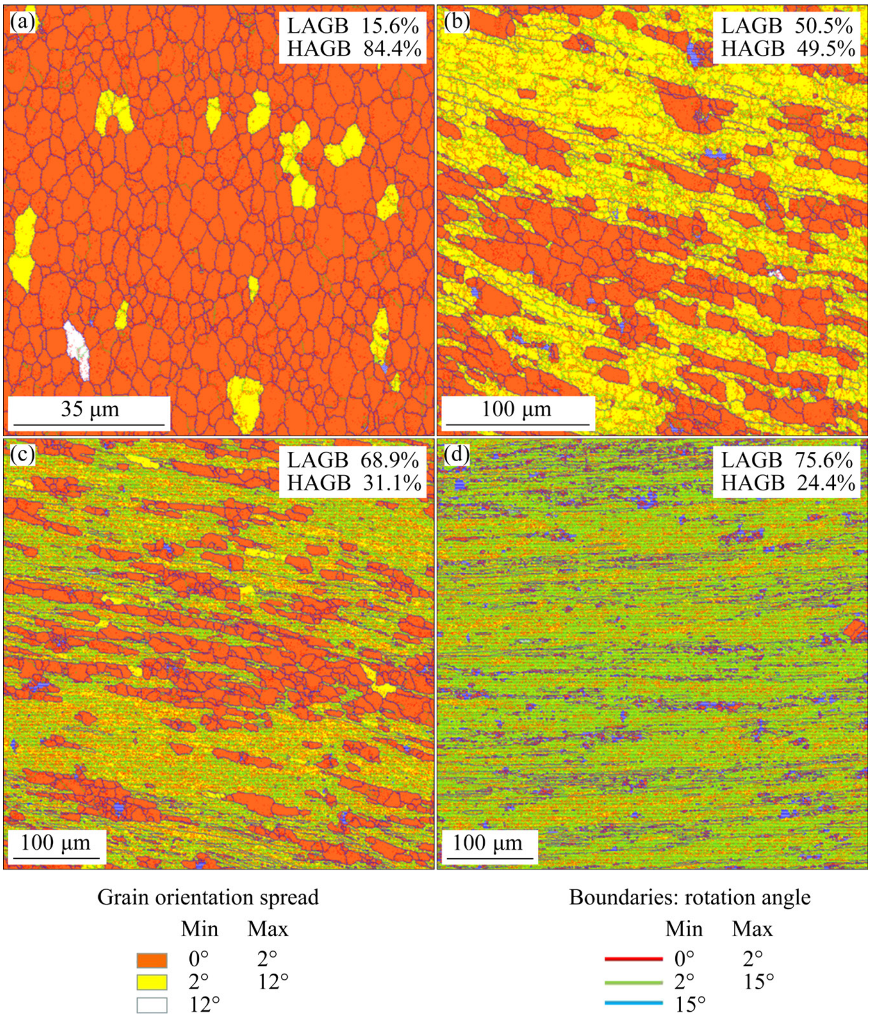

Fig. 4 GOS maps of different zones of DSFSWed joint of Al−Mg−Mn−Er alloy: (a) NZ; (b) TMAZ; (c) HAZ; (d) BM

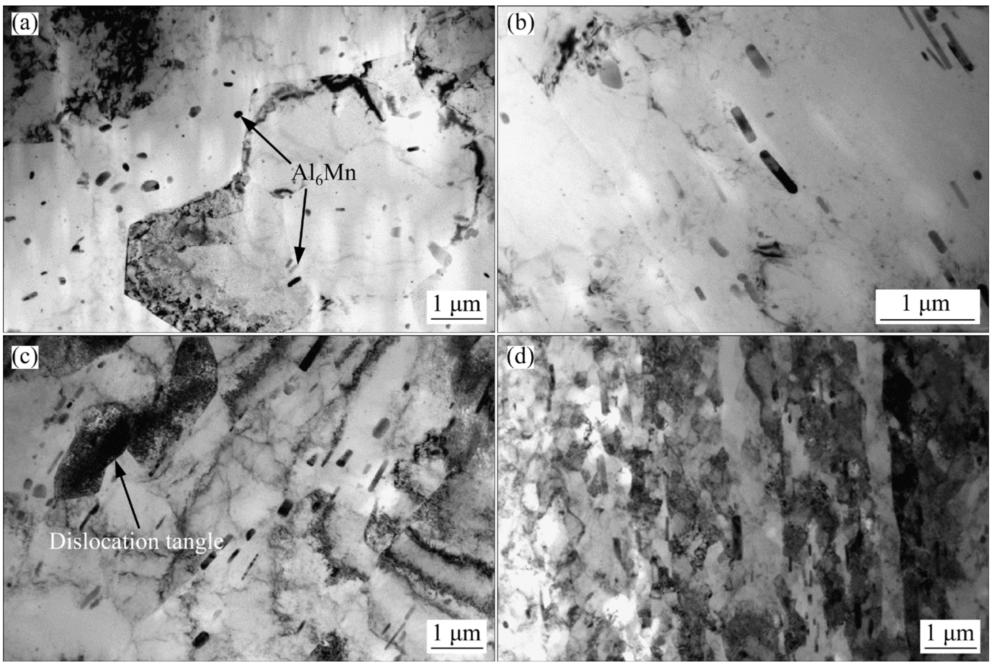

Fig. 5 Low magnification TEM images of DSFSWed joint of Al−Mg−Mn−Er alloy: (a) NZ; (b) TMAZ; (c) HAZ; (d) BM

distributed along the shearing direction and a number of dislocations are observed, as shown in Fig. 5(b). The HAZ shown in Fig. 5(c) occupies a high dislocation density due to relatively large distance between the observation position and the centerline of weld. Meanwhile, the Al_6Mn particles maintain distributed along the rolling direction. Figure 5(d) shows a hot-rolled microstructure of Al−Mg−Mn−Er alloy. The high-density dislocations, fibrous coarse grains, ultrafine grains and Al_6Mn particles arranged along the rolling direction are observed.

The high magnification TEM microstructure of the DSFSWed joint of Al−Mg−Mn−Er alloy is shown in Fig. 6. Figures 6(a−d) represent the NZ, TMAZ, HAZ and BM, respectively. The $Al_3(Er,Zr)$ precipitates are seen in all zones and form a relatively uniform distribution. The average

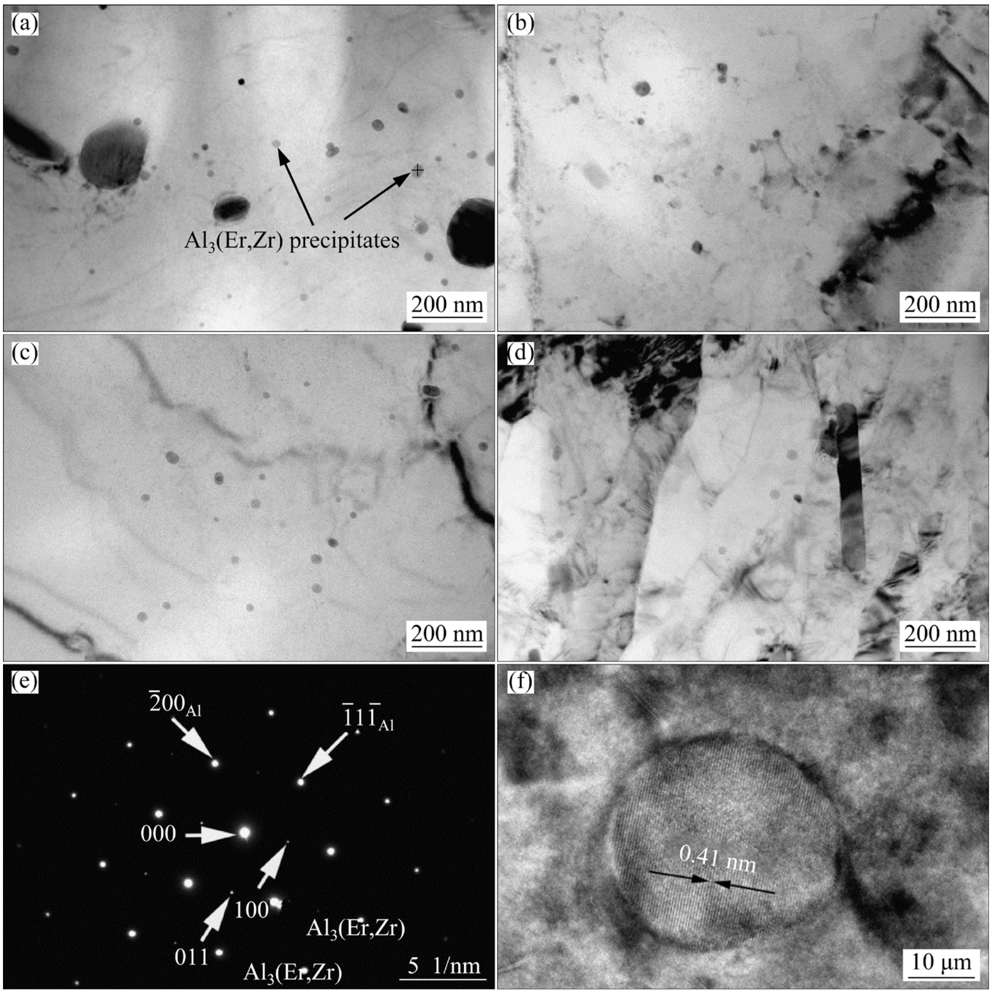

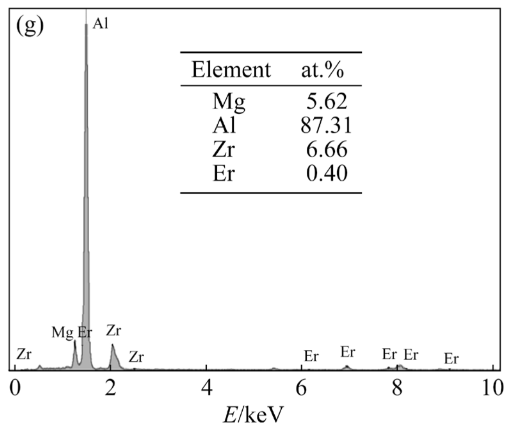

Fig. 6 High magnification TEM images of DSFSWed joint of Al−Mg−Mn−Er alloy: (a) NZ; (b) TMAZ; (c) HAZ; (d) BM; (e) Selective electron diffraction pattern; (f) HRTEM image; (g) EDS results

diameter sizes of $Al_3(Er,Zr)$ precipitates in the NZ, TMAZ, HAZ and BM are 14.0, 16.5, 15.3 and 13.7 nm, respectively. Although the NZ, TMAZ and HAZ experienced much heat input, the $Al_3(Er,Zr)$ precipitates maintained initial size and showed good thermal stability. Figures 6(e−g) show the selective electron diffraction pattern, HRTEM image and EDS results of $Al_3(Er,Zr)$ precipitates, respectively. Based on indexing the diffraction pattern and measuring the lattice constant, it is proved that the fine dispersive precipitates belong to $L1_2$ structure and the lattice constant is 0.42 nm. Combined with chemical composition (87.31 Al, 5.62 Mg, 6.66 Zr and 0.40 Er, at.%), it is determined that the fine dispersive precipitates are $Al_3(Er,Zr)$ precipitates. These observation results are consistent with the literature [25−27].

3.2 Mechanical properties

The yield strength profile of DSFSWed joint of Al−Mg−Mn−Er alloy is shown in Fig. 7. The distribution of yield strength forms a "U"-like shape. It indicates that the NZ is the softest zone with a yield strength of about 201 MPa, while the BM is the hardest zone with a yield strength of about 295 MPa. The yield strength of the TMAZ is close to that of the NZ. From the TMAZ to the BM, the yield strength of the HAZ increases from 205 to 280 MPa.

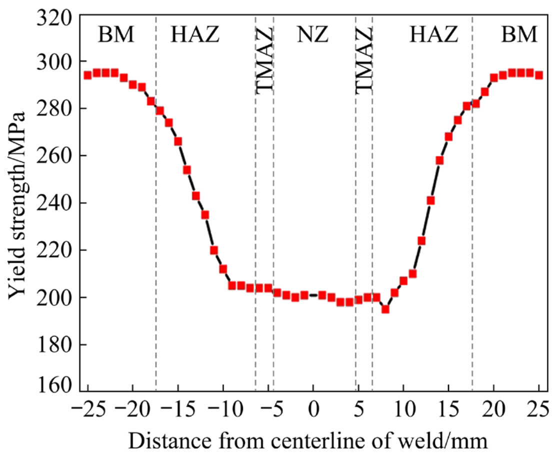

Fig. 7 Yield strength profile of DSFSWed joint of Al−Mg−Mn−Er alloy

Figure 8 shows the engineering stress−engineering strain curves and dynamic strain field (tensile direction) of the DSFSWed joint of Al−Mg−Mn−Er alloy. As the tensile stress increases, the tensile strain is increased and a few areas yield (ε>0.2%), as shown in Fig. 8(a). Further increasing the tensile stress causes the tensile strain field to form two areas with different degrees of strain, as shown in Fig. 8(b). A larger tensile strain is concentrated on the softer area including the NZ, TMAZ and a part of the HAZ. Meanwhile, the harder area consisting of the other part of the HAZ and the BM maintains a uniform tensile strain field. When the tensile stress further increases, the tensile strains of the softer and harder areas are increased, and the tensile strain increases at a larger rate in the softer area, as shown in Fig. 8(c). It means that a larger plastic strain occurs in the softer area. Figure 8(d) presents the initial stage of necking. Once necking occurs, the tensile strain is severely increased because of the reduction in the load-bearing area.

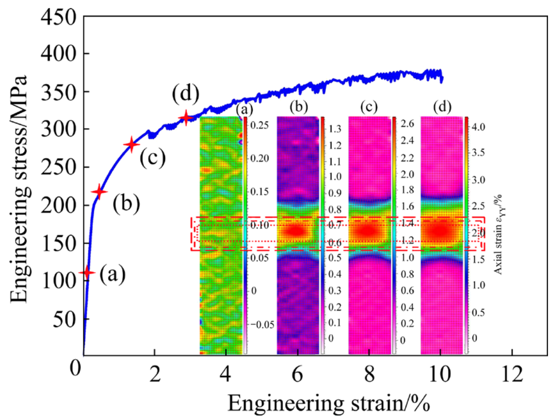

Fig. 8 Engineering stress−engineering strain curve and dynamic strain filed of DSFSWed joint of Al−Mg−Mn−Er alloy: (a) 20 s; (b) 46 s; (c) 86 s; (d) 116 s (The red dot line covers the NZ, the red dash dot line covers the TMAZ and the red dash line covers a part of HAZ)

4 Discussion

Different microstructures formed in the NZ, TMAZ, HAZ and BM during the DSFSW process due to different thermo-mechanical history. It led to an evolution of contributions of different strengthening mechanisms from the NZ to the BM. As known, the strengthening mechanism of metal materials could be expressed as follows [28]:

$$\sigma_{0.2}=\sigma_0+\sigma_s+\sigma_{GB}+\sigma_d+\sigma_p \tag{1}$$

where σ_0 is the intrinsic resistance to the motion of dislocations for pure aluminum, σ_s is the solid solution strengthening resulted from additional solid solution elements, σ_{GB} is the grain boundary strengthening, σ_d is the dislocation strengthening and σ_p is the precipitate strengthening. In the Al−Mg−Mn−Er alloy, Mg is the main solid solution strengthening element. Therefore, the σ_s could be expressed as follows [29]:

$$\sigma_s = H_{\mathrm{Mg}} C_{\mathrm{Mg}}^n \tag{2}$$

where H_{Mg} is the solid solution strengthening efficiency of Mg solutes, C_{Mg} is molar fraction of Mg, and n is a material constant. Considering the subgrain boundary strengthening effect, the grain boundary strengthening could be expressed as follows [30]:

$$\sigma_{\mathrm{GB}} = M\alpha G\sqrt{1.5b\left(\theta f S_{\mathrm{V}}\right)_{\mathrm{LAGB}}} + kd_{\mathrm{HAGB}}^{-1/2} \tag{3}$$

where M is the Taylor factor, α is a constant, θ is the mean misorientation angle of LAGBs, f is the fraction of LAGBs, and S_{V} is the area of LAGBs per unit volume. The dislocation strengthening is determined by the dislocation density and could be described by the Taylor equation [31]:

$$\sigma_d = M\alpha Gb\sqrt{\rho} \tag{4}$$

where ρ is the dislocation density. According to literature [25,32], the $Al_3(Er,Zr)$ precipitates with diameter size above 13.7 nm are unshearable. Therefore, the precipitate strengthening could be estimated according to the Orowan model [33]:

$$\sigma_p = 3.1 \times 0.84 \frac{Gb}{\lambda} \tag{5}$$

where G is the shear modulus of aluminum matrix, b is the magnitude of Burgers vector, and λ is the distribution spacing of $Al_3(Er,Zr)$ precipitates.

RYEN et al [29] found that at the yield point ε=0.002, the value of H simply reflects the solute effect on the strength. For Mg solid solute in Al−Mg series alloy, H=12.1 MPa·at.%$^{-n}$ and n=1.14 at a strain rate of 6×10^{-3} s^{-1}. According to literature [34], the correlation between yield stress and strain rate is weak in the range of 10^{-4}−10^{-3} s^{-1}. Therefore, the same H and n values were used in the present study. The Al−Mg−Mn−Er alloy could be analogous to the alloys defined by the literature [33] due to the existence of Mg solid solute and $Al_3(Er,Zr)$ precipitates. Thus, the same k value of 0.17 MPa·m$^{1/2}$ was used to calculate the grain boundary strengthening. The average Taylor factor of 3.1 was derived from OIM software. The shear modulus of 26.9 GPa was experimentally determined by KULITSKIY et al [35], and α is often valued at 0.24. Considering the similar chemical composition and the same type of Al_3X precipitates of the two alloys, the same shear modulus and α value were used. b=0.286 nm is the magnitude of Burgers vector for Al.

According to literature [33], σ_0 is approximately 10 MPa, and C_{Mg} is estimated to be 4 at.% in the NZ, TMAZ, HAZ and BM. As shown in Fig. 3, the average grain sizes of NZ, TMAZ, HAZ and BM are 5.61, 45.32, 100.73 and 73.01 μm, respectively. According to the EBSD statistical results, the θ_{LAGB} of the NZ, TMAZ, HAZ and BM is 0.007, 0.019, 0.023 and 0.034, respectively. The $S_{\mathrm{V}\,\mathrm{LAGB}}$ of the NZ, TMAZ, HAZ and BM is 1.1×10^5, 2.2×10^5, 4.2×10^5 and 8.7×10^5 m^{-1}, respectively. The f_{LAGB} of the NZ, TMAZ, HAZ and BM is 0.156, 0.505, 0.689 and 0.756, respectively. According to the results output by OIM software, the ρ_{GNDs} of the NZ, TMAZ, HAZ and BM are 4.5×10^{12}, 9.1×10^{13}, 1.2×10^{14} and 1.8×10^{14} m^{-2}, respectively. The distribution spacing of $Al_3(Er,Zr)$ precipitates could be calculated as follows [36]:

$$\lambda = 0.5D_{\mathrm{P}}\left(\sqrt{\frac{2\pi}{3f_{\mathrm{V}}}} - \frac{\pi}{4}\right) \tag{6}$$

where D_{P} is the average diameter size of $Al_3(Er,Zr)$ precipitates, and f_{V} is the volume fraction of $Al_3(Er,Zr)$ precipitates. According to IPP statistical results, the f_{V} of NZ, TMAZ, HAZ and BM is 0.0013, 0.0014, 0.0016 and 0.0013, respectively. The corresponding λ is 275, 290, 290 and 270 nm, respectively.

Based on the above coefficients and independent variables, the calculated yield strengths of the NZ, TMAZ, HAZ and BM are 231, 236, 258 and 302 MPa, respectively. The corresponding real yield strengths are 201, 205, 275 and 295 MPa, respectively. The calculated values have a good fitting relationship with the real values. The contributions of different strengthening mechanisms in the NZ, TMAZ, HAZ and BM are shown in Fig. 9. From the NZ to the BM, the absolute values of solid solution strengthening and precipitate strengthening show little difference, while their contributions gradually decrease from 25.5% to 19.5% and from 31.6% to 24.5%, respectively. The absolute value and the contribution (31.1% to 6.6%) of high angle grain boundary strengthening are severely decreased from the NZ to the BM. Both the absolute value and the contribution (2.2% to 20.5%) of subgrain boundary strengthening show an increasing trend from the NZ to the BM. Meanwhile, welding thermal cycle results in obvious reduction in dislocation strengthening effect in the NZ, while the TMAZ, HAZ and BM maintain significant dislocation strengthening effect.

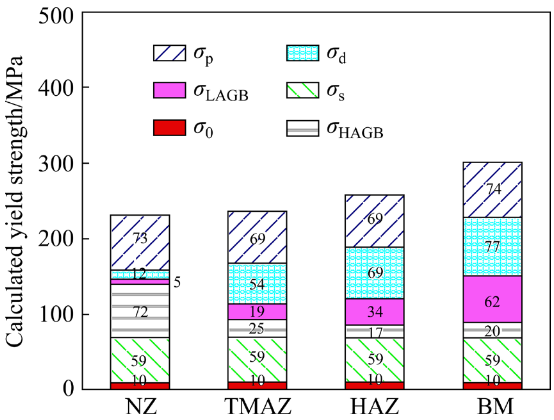

Fig. 9 Contribution of different strengthening mechanisms in NZ, TMAZ, HAZ and BM

The yield strength of the TMAZ is similar to that of the NZ. It is due to the fact that the loss of high angle grain boundary strengthening is offset by additional subgrain boundary strengthening and dislocation strengthening. It is worth noting that the HAZ under investigation is a specific area whose distance from the centerline of weld is about 16 mm. The whole HAZ covers a relative wide area with a length of 10 mm on each side of the joint. With the distance from the centerline of weld increasing, the annealing effect caused by welding thermal cycle is gradually weakened in the HAZ. More dislocations and subgrain boundaries are preserved. The absolute value and contribution of dislocation strengthening and subgrain boundary strengthening increase. Therefore, the yield strength of the HAZ shows an increasing trend from the TMAZ to the BM.

Based on the evolution of contributions of different strengthening mechanisms from the NZ to the BM, it is proved that the welding thermal cycle results in a loss of the yield strength in the softer area. Therefore, the yield occurred firstly in the softer area during the tensile process (Fig. 8). Compared to the harder area, there was less resistance to the dislocation slip owing to the loss of dislocations and subgrain boundaries. Moreover, the fine equiaxed grain structure of the NZ strengthened the coordination of deformation in the softer area. Thus, the softer area showed better ductility. In actual engineering application, the loss of yield strength is undesirable and appropriate welding process adjustment should be conducted to preserve as many dislocations and subgrain boundaries as possible.

5 Conclusions

(1) The NZ formed a fine equiaxed grain structure (5.61 μm) due to sufficient recrystallization. The TMAZ, HAZ and BM showed a fibrous grain structure and the average grain size increased from 45.32 μm of the TMAZ to 100.73 μm of the HAZ and then decreased to 73.01 μm of the BM due to different thermo-mechanical history. The fraction of LAGBs decreased from 75.6% of the BM to 15.6% of the NZ.

(2) The welding thermal cycle resulted in obvious reduction of dislocation densities from 1.8×10^{14} m^{-2} of the BM to 4.5×10^{12} m^{-2} of the NZ. The average diameter size and volume fraction of $Al_3(Er,Zr)$ precipitates of the NZ, TMAZ and HAZ were close to that of the BM (13.7 nm and 0.13%).

(3) The NZ occupied the lowest yield strength of 201 MPa due to obvious reduction of dislocation strengthening and subgrain boundary strengthening. The yield strength of TMAZ nearly equaled to that of the NZ, because the loss of high angle grain boundary strengthening was offset by additional dislocation strengthening and subgrain boundary strengthening. Due to more dislocations and subgrains preserved, the yield strength of the HAZ increased from 205 to 280 MPa.

(4) The NZ, TMAZ and a part of HAZ formed the softer area and the other part of HAZ and the BM formed the harder area during the tensile process. It is necessary to preserve as many dislocations and subgrain boundaries as possible to improve the yield strength of the softer area.

Acknowledgments

The present work is financially supported by the National Key Research and Development Program of China (No. 2020YFB0311203), and the Natural Science Foundation of Henan, China (No. 202300410005).

References

[1] ZHU Chen-xiao, TANG Xin-Hua, HE Yuan, LU Feng-gui,

CUI Hai-chao. Effect of preheating on the defects and microstructure in NG-GMA welding of 5083 Al-alloy [J]. Journal of Materials Processing Technology, 2018, 251: 214−224.

[2] WANG Qiang-tao, WANG Xiao-nan, CHEN Xia-ming, HUAN Peng-cheng, DONG Qi-peng, ZHANG Qing-yu, NAGAUMI H. Interactive effects of porosity and microstructure on strength of 6063 aluminum alloy CMT MIX + synchropulse welded joint [J]. Transactions of Nonferrous Metals Society of China, 2022, 32: 801−811.

[3] SALIH O S, NEATE N, OU Hen-gan, SUN W. Influence of process parameters on the microstructural evolution and mechanical characterisations of friction stir welded Al−Mg−Si alloy [J]. Journal of Materials Processing Technology, 2020, 275: 116366.

[4] DING Tian, YAN Hong-ge, CHEN Ji-hua, XIA Wei-jun, SU Bin. Effect of welding speed on microstructure and mechanical properties of Al−Mg−Mn−Zr−Ti alloy sheet during friction stir welding [J]. Transactions of Nonferrous Metals Society of China, 2021, 31: 3626−3642.

[5] CABIBBO M, FORCELLESE A, EL MEHTEDI M, SIMONCINI M. Double side friction stir welding of AA6082 sheets: Microstructure and nanoindentation characterization [J]. Materials Science and Engineering A, 2014, 590: 209−217.

[6] XU Wei-feng, LIU Jin-he. Microstructure evolution along thickness in double-side friction stir welded 7085 Al alloy [J]. Transactions of Nonferrous Metals Society of China, 2015, 25: 3212−3222.

[7] YANG C, ZHANG J F, MA G N, WU L H, ZHANG X M, HE G Z, XUE P, NI D R, XIAO B L, WANG K S, MA Z Y. Microstructure and mechanical properties of double-side friction stir welded 6082Al ultra-thick plates [J]. Journal of Materials Science and Technology, 2020, 41: 105−116.

[8] PENG Yong-yi, YIN Zhi-min, LEI Xue-feng, PAN Qing-lin, HE Zhen-bo. Microstructure and properties of friction stir welded joints of Al−Mg−Sc alloy plates [J]. Rare Metal Materials and Engineering, 2011, 40: 201−205.

[9] HAO H L, NI D R, HUANG H, WANG D, XIAO B L, NIE Z R, MA Z Y. Effect of welding parameters on microstructure and mechanical properties of friction stir welded Al−Mg−Er alloy [J]. Materials Science and Engineering A, 2013, 559: 889−896.

[10] MALOPHEYEV S, KULITSKIY V, MIRONOV S, ZHEMCHUZHNIKOVA D, KAIBYSHEV R. Friction-stir welding of an Al−Mg−Sc−Zr alloy in as-fabricated and work-hardened conditions [J]. Materials Science and Engineering A, 2014, 600: 159−170.

[11] CHEN Bin, CHEN Wen-peng, PAN Bing. High-precision video extensometer based on a simple dual field-of-view telecentric imaging system [J]. Measurement, 2020, 166: 108209.

[12] ZHU Fei-peng, LU Run-zhi, GU Jian, TAO Jin, BAI Peng-xiang, LEI Dong. High-resolution and high-accuracy optical extensometer based on a reflective imaging technique [J]. Optics and Lasers in Engineering, 2020, 132: 106136.

[13] WRIGHT S I, NOWELL M M, FIELD D P. A review of strain analysis using electron backscatter diffraction [J]. Microscopy and Microanalysis, 2011, 17: 316−329.

[14] KUBOTA M, USHIODA K, MIYAMOTO G, FURUHARA T. Analysis of recrystallization behavior of hot-deformed austenite reconstructed from electron backscattering diffraction orientation maps of lath martensite [J]. Scripta Materialia, 2016, 112: 92−95.

[15] CHAUDHURI A, BEHERA A N, SARKAR A, KAPOOR R, RAY R K, SUWAS S. Hot deformation behaviour of Mo-TZM and understanding the restoration processes involved [J]. Acta Materialia, 2019, 164: 153−164.

[16] LIAO Bin, CAO Ling-fei, WU Xiao-dong, ZOU Yan, HUANG Guang-jie, ROMETSCH P A, COUPER M J, LIU Qing. Effect of heat treatment condition on the flow behavior and recrystallization mechanisms of aluminum alloy 7055 [J]. Materials, 2019, 12(2): 311.

[17] IMANIAN GHAZANLOU S, EGHBALI B, PETROV R. EBSD characterization of Al7075/graphene nanoplates/ carbon nanotubes composites processed through post-deformation annealing [J]. Transactions of Nonferrous Metals Society of China, 2021, 31: 2250−2263.

[18] GAO H, HUANG Y, NIX W D, HUTCHINSON J W. Mechanism-based strain gradient plasticity—I. Theory [J]. Journal of the Mechanics and Physics of Solids, 1999, 47: 1239−1263.

[19] KUBIN L P, MORTENSEN A. Geometrically necessary dislocations and strain-gradient plasticity: A few critical issues [J]. Scripta Materialia, 2003, 48: 119−125.

[20] CALCAGNOTTO M, PONGE D, DEMIR E, RAABE D. Orientation gradients and geometrically necessary dislocations in ultrafine grained dual-phase steels studied by 2D and 3D EBSD [J]. Materials Science and Engineering A, 2010, 527: 2738−2746.

[21] LENG Jin-feng, REN Bing-hui, ZHOU Qing-bo, ZHAO Ji-wei. Effect of Sc and Zr on recrystallization behavior of 7075 aluminum alloy [J]. Transactions of Nonferrous Metals Society of China, 2021, 31: 2545−2557.

[22] CHEN Y W, TSAI Y T, TUNG P Y, TSAI S P, CHEN C Y, WANG S H, YANG J R. Phase quantification in low carbon Nb−Mo bearing steel by electron backscatter diffraction technique coupled with kernel average misorientation [J]. Materials Characterization, 2018, 139: 49−58.

[23] BIROL Y, KASMAN S. Effect of welding parameters on microstructure and mechanical properties of friction stir welded EN AW 5083 H111 plates [J]. Materials Science and Technology, 2013, 29: 1354−1362.

[24] SATO Y S, TAKAUCHI H, PARK S H C, KOKAWA H. Characteristics of the kissing-bond in friction stir welded Al alloy 1050 [J]. Materials Science and Engineering A, 2005, 405: 333−338.

[25] MOCHUGOVSKIY A G, MIKHAYLOVSKAYA A V, TABACHKOVA N Y, PORTNOY V K. The mechanism of $L1_2$ phase precipitation, microstructure and tensile properties of Al−Mg−Er−Zr alloy [J]. Materials Science and Engineering A, 2019, 744: 195−205.

[26] SUN Shun-ping, LI Xiao-ping, YANG Jie, WANG Hong-jin, JIANG Yong, YI Dan-qing. Point defect concentrations of $L1_2$-Al_3X(Sc,Zr,Er) [J]. Rare Metals, 2018, 37: 699−706.

[27] DING Yu-sheng, WU Xiao-lan, GAO Kun-yuan, HUANG Cheng, XIONG Xiang-yuan, HUANG Hui, WEN Shen-ping, NIE Zuo-ren. The influence of stabilization treatment on

long-term corrosion resistance and microstructure in Er and Zr containing 5083 aluminum alloy [J]. Materials Characterization, 2020, 161: 110143.
[28] FANG Hong-jie, LIU Hui, YAN Yang, LUO Xi-er, XU Xiang-chun, CHU Xin, LU Yu-jiao, YU Kun, WANG Dian-gang. Evolution of texture, microstructure, tensile strength and corrosion properties of annealed Al−Mg−Sc−Zr alloys [J]. Materials Science and Engineering A, 2021, 804: 140682.
[29] RYEN Ø, HOLMEDAL B, NIJS O, NES E, SJÖLANDER E, EKSTRÖM H E. Strengthening mechanisms in solid solution aluminum alloys [J], Metallurgical and Materials Transactions A, 2006, 37(6): 1999−2006.
[30] HANSEN N. Hall−Petch relation and boundary strengthening [J]. Scripta Materialia, 2004, 51: 801−806.
[31] ZHA M, LI Y J, MATHIESEN R H, BJØRGE R, ROVEN H J. Microstructure evolution and mechanical behavior of a binary Al−7Mg alloy, processed by equal-channel angular pressing [J]. Acta Materialia, 2015, 84: 42−54.
[32] LEFEBVRE W, MASQUELIER N, HOUARD J, PATTE R, ZAPOLSKY H. Tracking the path of dislocations across ordered Al_3Zr nano-precipitates in three dimensions [J]. Scripta Materialia, 2014, 70: 43−46.
[33] KENDIG K L, MIRACLE D B. Strengthening mechanisms of an Al−Mg−Sc−Zr alloy [J]. Acta Materialia, 2002, 50: 4165−4175.
[34] MUKAI T, HIGASHI K, TANIMURA S. Influence of the magnesium concentration on the relationship between fracture mechanism and strain rate in high purity Al−Mg alloys [J]. Materials Science and Engineering A, 1994, 176: 181−189.
[35] KULITSKIY V, MALOPHEYEV S, MIRONOV S, KAIBYSHEV R. Grain refinement in an Al−Mg−Sc alloy: Equal channel angular pressing versus friction-stir processing [J]. Materials Science and Engineering A, 2016, 674: 480−490.
[36] KNIPLING K E, DUNAND D C, SEIDMAN D N. Precipitation evolution in Al−Zr and Al−Zr−Ti alloys during aging at 450−600 °C [J]. Acta Materialia, 2008, 56: 1182−1195.

Al−Mg−Mn−Er 合金双面搅拌摩擦焊接头局部显微组织和强化机制

刘海彬，王腾达，刘国元，谢述锋，褚少旗，谢 斌，杨胜利，王鹏云

洛阳船舶材料研究所，洛阳 471023

摘 要：通过研究 Al−Mg−Mn−Er 合金双面搅拌摩擦焊接头的局部显微组织和强化机制揭示其软化机制。结果显示：焊核区形成细小等轴晶组织(5.61 μm)，而热机械影响区(45.32 μm)和热影响区(100.73 μm)仍为纤维状组织。从基体到焊核区，小角度晶界分数从 75.6%降低到 15.6%。退火效应导致位错密度从母材的 1.8×10^{14} m^{-2} 减小到焊核区的 4.5×10^{12} m^{-2}。焊核区、热机械影响区和热影响区 $Al_3(Er,Zr)$析出相的平均尺寸和体积分数与基体的(13.7 nm，0.13%)均接近。焊核区和热机械影响区的屈服强度最低，约为 201 MPa；基体的屈服强度最高，约为 295 MPa。位错强化和亚结构强化的损失是从基体到焊核区屈服强度降低的主要原因。

关键词：Al−Mg−Mn−Er 合金；双面搅拌摩擦焊；显微组织；强化机制

(Edited by Xiang-qun LI)